Journal Name

ARTICLE TYPE

Cite this: DOI: 10.1039/xxxxxxxxxx

Tailoring Spin Dynamics through Proximity Effects in Graphene/Transition Metal Dichalcogenide Heterostructures†

Jose H Garcia,*[a], Marc Vila,*[a], Aron W Cummings,*[a] and Stephan Roche[ab]‡

Received Date
Accepted Date

DOI: 10.1039/xxxxxxxxxx

www.rsc.org/journalname

Since its discovery, graphene has been a promising material for spintronics: its low spin-orbit coupling, negligible hyperfine interaction, and high electron mobility are obvious advantages for transporting spin information over long distances. However, such outstanding transport properties also limit the capability to engineer active spintronics, where strong spin-orbit coupling is crucial for creating and manipulating spin currents. To this end, transition metal dichalcogenides, which have larger spin-orbit coupling and good interface matching, appear to be highly complementary materials for enhancing the spin-dependent features of graphene while maintaining its superior charge transport properties. In this review, we present the theoretical framework and the experiments performed to detect and characterize the spin-orbit coupling and spin currents in graphene/transition metal dichalcogenide heterostructures. Specifically, we will concentrate on recent measurements of Hanle precession, weak antilocalization and the spin Hall effect, and provide a comprehensive theoretical description of the interconnection between these phenomena. Finally, to complete the perspective of graphene-based heterostructures for spintronics, other recent and less explored systems such as graphene coupled with topological insulators will be briefly discussed.

1 Introduction

Graphene, a two dimensional carbon allotrope, has proven over the last decade to be a truly wonder material. Despite its simple structure and chemical composition, its use in a variety of fields such as coatings, sensors, energy, biomedicine, photonics, and optoelectronics has demonstrated the richness of its properties and its potential industrial impact[1]. The usefulness of graphene for spintronics has also been recognized, owing to its high electron mobility[2–4], small spin-orbit coupling (SOC)[5–8] and negligible hyperfine interaction[9,10]. All together these factors result in coherent spin propagation over unprecedented microscopic distances[11–15], proving graphene to be a suitable enabling material for passive spin components[16].

Additionally, an increasing body of evidence shows that SOC in graphene can be enhanced through interaction with a substrate or with adatoms[17–28], opening a path for the implementation of active graphene-based spintronic devices. Between these two approaches, high-SOC substrates are preferred[23–26] because they are chemically inert and electrically insulating, and thus will have little impact on graphene's electronic properties. Meanwhile, weak hybridization with the substrate can enhance the SOC in the graphene layer, potentially leading to predicted phenomena such as the spin Hall effect (SHE)[29,30] or the quantum spin Hall effect[31]. Experiments carried out over the past few years have reported strong evidence of such proximity-induced SOC enhancement in graphene when interfaced with transition metal dichalcogenides (TMDCs), and new spin device functionalities have been proposed[19,20,23–26]. Therefore, an in-depth understanding and characterization of the properties of graphene/TMDC heterostructures appears to be fundamental for the field of spintronics.

The materials used in spintronics applications can be characterized by three fundamental figures of merit: the spin relaxation time τ_s, the spin diffusion length λ_s, and the spin Hall angle γ_{sH}. The relaxation time dictates the upper time limit within which spin information can be transmitted and manipulated, hence large τ_s is desired. The spin diffusion length denotes the distance over which spin currents can propagate without losing information, and must also be maximized. Both quantities are related by the spin diffusion coefficient D_s, which depends on the sample mobility and the transport regime, and is given

[a] Catalan Institute of Nanoscience and Nanotechnology (ICN2), CSIC and BIST, Campus UAB, Bellaterra, 08193 Barcelona, Spain.; E-mail: josehugo.garcia@icn2.cat
[b] ICREA - Institució Catalana de Recerca i Estudis Avançats, 08010 Barcelona, Spain.

† Electronic Supplementary Information (ESI) available: [details of any supplementary information available should be included here]. See DOI: 10.1039/b000000x/

‡ Additional footnotes to the title and authors can be included *e.g.* 'Present address:' or 'These authors contributed equally to this work' as above using the symbols: ‡, §, and ¶. Please place the appropriate symbol next to the author's name and include a `\footnotetext` entry in the the correct place in the list.

in the diffusive regime by $\lambda_s = \sqrt{D_s \tau_s}$. Finally, the spin Hall angle, which is the figure of merit of the spin Hall Effect[32], measures the efficiency of charge-to-spin conversion and vice versa. This quantity must be maximized for practical use in data storage or future non-charge-based information processing technologies. These parameters are usually evaluated through three different types of experiments: (i) measurements of Hanle precession in lateral spin valves, (ii) measurements of the weak antilocalization effect, and (iii) measurements of magnetic-field-modulated nonlocal resistance in Hall bar geometries. Each of these approaches yields some combination of τ_s, λ_s, and γ, but the obtained values can differ depending on the measurement technique. This has led to some apparent contradictions when compared to the available theoretical framework, and calls for a better understanding of these phenomena and the relationship between them in order to move forward into practical applications.

In this review, we present a unified description of graphene/TMDC heterostructures in the context of spintronics, through a discussion of some of the most relevant experiments and their relationship to recent theoretical developments. The review is organized as follows: Section 2 starts with an introduction to spin transport measurements performed in graphene supported on silicon oxide and hexagonal boron nitride (hBN) substrates. Additionally, we give an overview of the most relevant evidence of spin-orbit coupling enhancement in graphene and how it was determined. Both of these discussions will serve as a baseline for understanding new results in graphene/TMDC systems. In Section 3 we introduce the theory of spin-orbit coupling and spin relaxation in graphene/TMDC heterostructures, which will be used to interpret and analyze the measurements discussed in the following sections. In Section 4, we discuss the theory of Hanle precession in lateral spin valves and its extension to anisotropic systems. We then use the theoretical framework presented in Section 3 and the Hanle precesson theory to offer some insights into recent experimental results. In Section 5 we review weak antilocalization (WAL) theory, summarize the measurements of WAL in graphene/TMDC heterostructures, and comment on the need to consider valley-Zeeman SOC in the analysis of these measurements. We also discuss the limits of traditional WAL analysis in systems with very strong SOC. In Section 6 we present a basic introduction of the spin Hall effect and we discuss the complexity of the phenomenon in graphene/TMDC heterostructures. Then we discuss numerical predictions of the SHE in these systems and propose some methods for its experimental observation. The Rashba-Edelstein effect is also briefly discussed. The review concludes in Section 7, where we highlight the main take-home messages and offer some perspectives for the future of these devices, as well as for graphene interfaced with other SOC.

2 History of spin transport in graphene

2.1 Graphene on traditional substrates

Owing to its small spin-orbit coupling and hyperfine interaction[5–10], graphene is expected to possess long spin relaxation times τ_s and lengths λ_s. Indeed, the first theoretical studies predicted τ_s exceeding the μs range[33–35], which is orders of magnitude larger than in typical metals and semiconductors[36]. These estimates were based on traditional mechanisms of spin relaxation in metals and semiconductors, namely the Elliot-Yafet (EY) and D'yakonov-Perel' (DP) mechanisms. In the EY mechanism[37,38], an electron's spin has a finite probability of flipping during a scattering event, leading to a spin relaxation time that is proportional to the momentum scattering time τ_p. In graphene this relation is given as $\tau_s = (2E_F/\lambda)^2 \tau_p$, where λ is the SOC strength and E_F is the Fermi energy[39]. In the DP mechanism[40], SOC leads to electron spin precession and dephasing between scattering events. When the scattering time is shorter than the precession time, electrons tend to maintain their spin orientation, in what is known as motional narrowing. This leads to a spin relaxation time that is inversely proportional to the momentum scattering time, $\tau_s = (\hbar/2\lambda)^2/\tau_p$, where $\hbar$ is the reduced Planck constant. In combination with the small SOC in graphene, these mechanisms are predicted to give very long spin relaxation times[10].

The nonlocal Hanle spin precession measurement is the typical experimental technique employed to study spin relaxation in graphene, as it allows the extraction of both τ_s and λ_s[41–43]. Early measurements of graphene spin valves revealed $\tau_s < 1$ ns[11,44–50], while the use of hBN as a substrate or protective layer, in addition to other improvements of device quality, have yielded spin lifetimes up to 12 ns[12,15,51–53]. Although these results already make clean graphene a suitable platform for achieving longer coherent spin propagation than in typical metals or semiconductors, τ_s remains several orders of magnitude below the initial theoretical predictions[33–35], a puzzling result which remains open to discussion and interpretation[13,16]. Indeed, this intriguing difference between theory and experiment initially suggested that the DP and EY mechanisms may not be fully appropriate for graphene.

As a result, different mechanisms have recently been proposed to explain this discrepancy, including scattering by magnetic impurities in dirtier samples[54–56], or the role played by spin-pseudospin coupling in the ultraclean limit, which may be found in hBN-encapsulated devices[57–59]. To determine which mechanism is responsible for spin relaxation, experiments typically probe the dependence of τ_s and λ_s on the applied gate voltage, electron density, sample quality, or measurement temperature[10,48]. Unfortunately, it remains difficult to unambiguously differentiate one relaxation mechanism from another, given the complex relation between spin dynamics, disorder, and substrate-induced spin-orbit effects[13].

For this reason, recent studies have focused on the evaluation of spin lifetime anisotropy ζ, defined as the ratio of the lifetime of spins pointing out of the graphene plane to those pointing in the plane. Different spin relaxation mechanisms yield different anisotropy values, making this quantity a useful probe of the nature of the spin dynamics in a given system. For example, the DP mechanism driven by Rashba SOC[60] in disordered two-dimensional systems yields $\zeta = 1/2$[42], while magnetic impurities[55,56] and the spin-pseudospin coupling mechanism[57,58] both produce $\zeta = 1$. Recent measurements of graphene on SiO_2 substrates[61,62] have revealed $\zeta = 1$. This rules out Rashba SOC as the driver of spin relaxation mechanism in graphene, but more work

is needed in order to discriminate between magnetic impurities and spin-pseudospin coupling.

2.2 Enhancement of SOC in graphene

Recently, a three-order-of-magnitude enhancement of SOC was reported in weakly hydrogenated graphene[17]. Subsequently, a large number of experiments have also reported evidence of SOC enhancement in graphene, opening a new era for graphene-based spintronics[17–20,23–26,63–68]. The presence of spin-orbit coupling in a material can be detected by measuring weak antilocalization or the spin Hall effect, as in general these phenomena will not exist without SOC*. The first experimental measurements were focused on detecting the spin Hall effect through measurements of nonlocal resistance in a Hall bar geometry. Such measurements indeed found large nonlocal signals, and these were attributed to enhancement of the SOC in graphene by adatoms[17,18,20]. However, using this approach can be complicated given that a variety of phenomena unrelated to spin may also lead to large nonlocal signals[27,28,70–72]

In graphene/TMDC heterostructures, the initial measurements were centered on detecting weak antilocalization, which is then fitted to WAL theory[73] to obtain the corresponding spin relaxation rates. Following this approach, a variety of groups have confirmed the undeniable presence of proximity-induced SOC[19,23,24,26,63,64,67,68]. SOC parameters can be indirectly evaluated from WAL measurements by connecting spin-orbit relaxation rates to spin relaxation mechanisms. However, all but the most recent analyses have ignored the impact of valley-Zeeman SOC, despite simulations based on density functional theory (DFT) showing it to be the dominant term[63,64,74,75]. Finally, it was recently proposed that a giant spin lifetime anisotropy is a signature of proximity-induced SOC in graphene/TMDC heterostructures[76]. This effect was subsequently confirmed by two independent groups using variations of the Hanle precession measurement[65,66]. These measurements make it clear that TMDCs induce a strong SOC in graphene, and that the nature of this SOC leads to unusual features in the spin transport. In the following section we provide the theoretical framework to understand the nature of spin transport in these systems.

3 Theory of graphene/TMDC heterostructures

In the past two years, clear signatures of proximity-induced SOC have been measured in graphene/TMDC heterostructures[18,19,21,24,26,64]. In parallel, these systems have been studied with *ab initio* methods[63,64,74,75], which yield quite consistent results: a SOC strength on the order of 1 meV, the presence of Rashba SOC, and the appearance of a new type of SOC denoted valley-Zeeman SOC[64], which turns out to dominate over the other ones. These calculations also predicted that among all the TMDCs, WS_2, WSe_2, MoS_2, and $MoSe_2$ are the most suitable to be used as enabling substrates, given their imprint on the low-energy electronic properties of graphene and the absence of mixing with high-energy bands of the TMDC semiconductors[74].

3.1 Electronic model

To capture the main features of the *ab initio* calculations, a tight-binding (TB) model was developed using group theory by Gmitra and coworkers[74,77]. In this model, all SOC terms allowed by symmetry are incorporated in the graphene Hamiltonian, and by fitting the electronic structure and spin texture to the *ab initio* results, the strength of the various SOC parameters can be estimated. The model is given as

$$H = H_{\rm orb} + H_{\rm so}, \tag{1}$$

where the first term

$$H_{\rm orb} = \hbar v_{\rm F} \left(\kappa \sigma_x k_x + \sigma_y k_y\right) + \Delta \sigma_z \tag{2}$$

represents the orbital part of the Hamiltonian, described by the Dirac equation with $v_{\rm F}$ the Fermi velocity, σ_i the Pauli matrices acting on the pseudospin subspace, $\kappa = 1(-1)$ for the K (K′) valley, and Δ a mass term arising from a weak superlattice effect induced by the TMDC[74,77]. The second term,

$$H_{\rm so} = H_R + H_{PIA} + H_I + H_{VZ} + H_{\Delta PIA}, \tag{3}$$

with

$$\begin{aligned} H_R &= \lambda_R(\sigma_x s_y - \sigma_y s_x), \\ H_{PIA} &= a\lambda_{PIA}\sigma_z(k_x s_y - k_y s_x), \\ H_I &= \lambda_I \kappa \sigma_z s_z, \\ H_{VZ} &= \lambda_{VZ} \kappa s_z, \\ H_{\Delta PIA} &= a\lambda_{\Delta PIA}(k_x s_y - k_y s_x), \end{aligned} \tag{4}$$

represents the proximity-induced enhancement of SOC. The first element is a Rashba SOC with strength λ_R, arising from a perpendicular electric field. H_{PIA} is a SOC that appears due to the absence of horizontal reflection symmetry and which renormalizes the Fermi velocity. H_I is the intrinsic SOC in graphene, which opens a topological gap $2\lambda_I$ at the Dirac point[31]. H_{VZ} is a valley-Zeeman term, which spin polarizes the bands out of the graphene plane with opposite orientation in the K and K′ valleys, also known as spin-valley locking. Finally, $H_{\Delta PIA}$ is a second-order Rashba term that causes a k-linear splitting of the bands, as in traditional 2D electron gases (2DEGs) with Rashba SOC[60]. Except for the PIA terms, this Hamiltonian is the same as that considered in other works[21,24,64,75]. The values of these parameters are on the order of ∼1 meV except for the intrinsic SOC, which remains on the order of a few tens of μeV, similar to pristine graphene[74].

In Fig. 1, we show a comparison between graphene with only the typical Rashba SOC, and graphene in proximity to WS_2. In both cases the spin-orbit coupling produces very similar spin

* In this regard, graphene is a special case because there can be weak antilocalizaton due to the presence of pseudospin[69]. However, this happens under very special experimental conditions which are not the general situation.

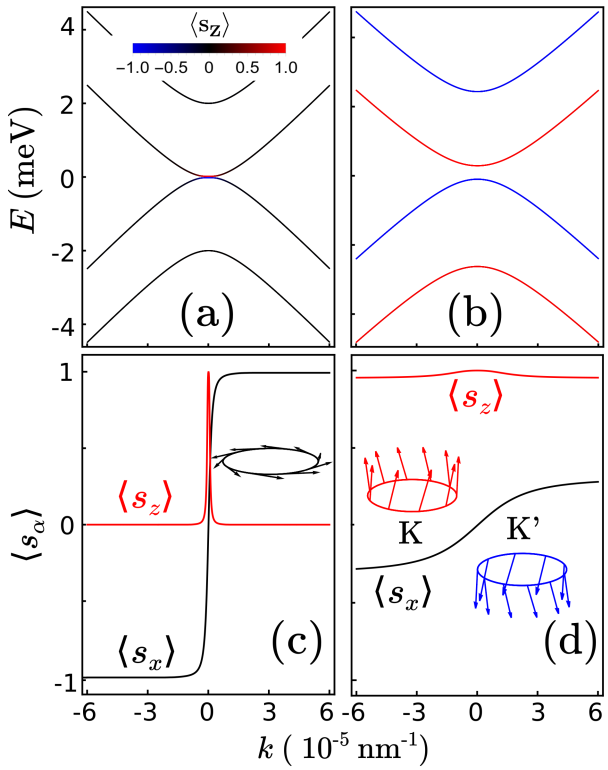

Fig. 1 Band structure of graphene (a) with only Rashba SOC and (b) in proximity to WS_2, where the color indicates the out-of-plane spin component. The splitting is quite similar but due to the presence of valley-Zeeman SOC there is a noticeable change in the spin texture, which is shown in panel (c) for Rashba SOC and panel (d) for WS_2 substrate. The insets show the spin texture at a given Fermi energy for both cases.

splitting, but it also induces very different spin textures. For pure Rashba SOC, the splitting is accompanied by an in-plane spin texture associated with spin-momentum locking. For the graphene/TMDC case, the valley-Zeeman term induces an effective out-of-plane magnetic field which tilts the spin texture in the perpendicular direction, with opposite direction in each valley. This difference will have major implications for the spin relaxation, weak antilocalization, and the spin Hall effect, as we will show in the following sections. This result also highlights the importance of the spin texture when fitting from *ab initio* data.

3.2 Microscopic theory of spin relaxation

When electrons propagate in a solid, the typical approximation is to consider the spin as an inactive internal degree of freedom. However, in the presence of spin-orbit coupling this is not the case, as the coupling of spin with momentum implies that the spin now can play a role in transport and be affected by scattering. The actual spin dynamics will depend on the disorder profile and the nature of the spin-orbit coupling. In graphene/TMDC heterostructures, experimental results suggest that the relaxation mechanism occurs in the D'yakonov-Perel' regime[26,63,64,78], where the spin precession of the electrons is interrupted by scattering events, inducing motional narrowing. However, due to the different SOC fields, the scaling of the relaxation times against momentum scattering time, as well as the relative magnitude between in-plane and out-of-plane relaxation times, present drastic changes compared to the pristine case[76].

In general, spin relaxation theory assumes the electrons belong to a single electronic band, which is split by the effect of the SOC field. Because of the existence of the two valleys in graphene, the typical theory is not directly applicable, especially in the presence of intervalley scattering. This difficulty can be overcome by performing an downfolding of the bands[79], which is done by expressing H in the basis of the eigenstates of $H_{\rm orb}$ followed by a projection onto the conduction and valence bands. At Fermi energies away from the Dirac point, this gives

$$H = H_{orb} + \frac{1}{2}\hbar\vec{\omega}(t)\cdot\vec{s}, \tag{5}$$

with $\vec{\omega}$ the spin precession frequency of the effective spin-orbit field, whose components are

$$\begin{aligned}\hbar\omega_x &= -2(ak\Delta_{PIA} \pm \lambda_R)\sin\theta,\\ \hbar\omega_y &= 2(ak\Delta_{PIA} \pm \lambda_R)\cos\theta,\\ \hbar\omega_z &= 2\kappa\lambda_{VZ},\end{aligned} \tag{6}$$

where k is the wave vector magnitude and θ is the direction of k with respect to k_x. The in-plane components of $\vec{\omega}$ give a Rashba-like spin texture, where $+(-)$ is for the conduction (valence) band. The out-of-plane component of $\vec{\omega}$ is determined by λ_{VZ} and changes sign between valleys.

Owing to the presence of momentum scattering, each component of $\vec{\omega}$ will fluctuate in time. If this fluctuation is uncorrelated, then the electron will not have any memory of its previous magnetic field, leading to a randomization of its spin. In the simplest model, the correlation time can be assumed as being the same as the momentum scattering time. However, the presence of the valley-Zeeman SOC means that intervalley scattering can also enhance spin randomization, but only of the in-plane spin component[76]. Based on these considerations, and assuming the DP regime, the relaxation rates of the out-of-plane and in-plane spins are

$$\begin{aligned}\left(\tau_s^{\perp}\right)^{-1} &= \left(2\frac{ak\Delta_{PIA} \pm \lambda_R}{\hbar}\right)^2 \tau_p,\\ \left(\tau_s^{\parallel}\right)^{-1} &= \left(\frac{2\lambda_{VZ}}{\hbar}\right)^2 \tau_{iv} + \frac{1}{2}\left(\tau_s^{\perp}\right)^{-1}.\end{aligned} \tag{7}$$

The out-of-plane spin thus follows a typical Rashba-induced relaxation process, with an electron-hole asymmetric behavior that originates from the PIA SOC. Meanwhile, because $\tau_{iv} > \tau_p$ by definition and typically $\lambda_{VZ} > \lambda_R$, the in-plane relaxation rate is dominated by the valley-Zeeman SOC, and converges to the typical Rashba behavior only when intervalley scattering or valley-Zeeman SOC are absent. Experimentally, the effect of PIA has not been observed, which could be an indication that in real systems this effect is somehow suppressed. For that reason, we neglect it and present the final expression for the spin lifetime anisotropy

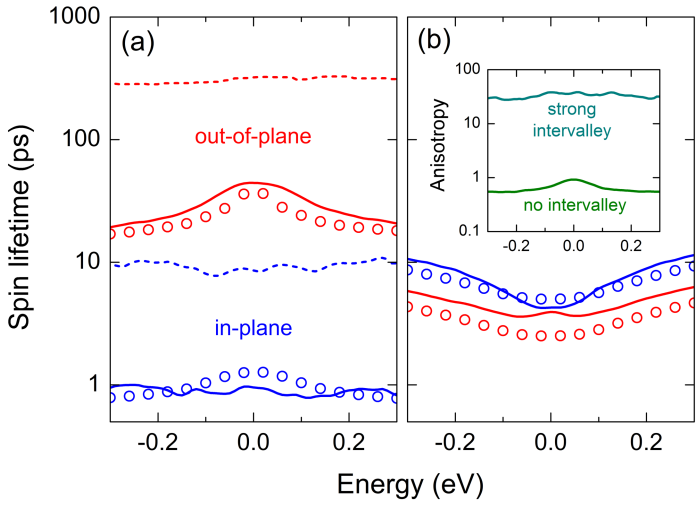

Fig. 2 Numerical simulations of the in-plane (blue) and out-of-plane (red) spin lifetimes for (a) strong intervalley scattering, and (b) weak intervalley scattering. In the inset we show the spin lifetime anisotropy for these two cases. Reproduced from Ref. 76.

considering only Rashba and valley-Zeeman SOC,

$$\zeta \equiv \frac{\tau_s^\perp}{\tau_s^\parallel} \approx \left(\frac{\lambda_{VZ}}{\lambda_R}\right)^2 \left(\frac{\tau_{iv}}{\tau_p}\right) + \frac{1}{2}. \tag{8}$$

Using DFT values of $\lambda_{VZ} = 1.2$ meV and $\lambda_R = 0.56$ meV for graphene on WSe_2[74], and assuming relatively strong intervalley scattering ($\tau_{iv} \sim 5\tau_p$), we obtain a spin lifetime anisotropy of $\zeta \approx 20$. This result is drastically different from the anisotropies found in graphene on SiO_2 or hBN substrates[51,61,62], where $\zeta \approx 1$. Thus, a giant anisotropy should be an experimental fingerprint of SOC proximity effects induced in graphene by TMDCs.

In Fig. 2 we present a numerical simulation of spin lifetimes in graphene on WSe_2. The simulations were performed considering electron-hole puddle disorder that is characterized by the puddle height U_p and the puddle concentration n, with the puddle width fixed to three lattice constants. For $U_p = 2.8$ eV and $n = 0.1\%$ these puddles produce strong intervalley scattering[80], which according to our theory should induce giant anisotropy. This is indeed the case, as shown in Fig. 2(a), where we find $\tau_s^\perp = 20 - 50$ ps and $\tau_s^\parallel \approx 1$ ps. The open circles are the values of τ_s estimated from Eq. (7), showing good agreement between the numerical simulations and the spin dynamics model. As shown by the dashed lines, increasing the disorder density to $n = 1\%$ scales τ_s by a factor of 10, showing that the inverse relationship between τ_s and $\tau_{p,iv}$ holds.

The in-plane spin relaxation rate in Eq. (7) was derived assuming the motional narrowing regime, when intervalley scattering is strong. When intervalley scattering is weak this assumption no longer applies and the first term in the expression for $1/\tau_s^\parallel$ disappears, leading to $\zeta = 1/2$. Figure 2(b) shows the case for weak intervalley scattering, where we see that the anisotropy indeed collapses toward 1/2. The inset of Fig. 2(b) shows the comparison between the anisotropy for weak and strong intervalley scattering. These results highlight the strong connection between intervalley scattering and the in-plane spin lifetime in graphene/TMDC heterostructures.

In this section, we presented a theoretical framework for spin relaxation in graphene/TMDC heterostructures, and showed that spin lifetime anisotropy is an undeniable fingerprint of proximity-induced SOC in graphene by the TMDC. However, the typical Hanle setup used to measure spin relaxation in graphene only probes the in-plane spin relaxation, and gives zero information about the out-of-plane component. Therefore, in the following section we will review a generalized Hanle measurement that allows for the detection of both the in-plane and out-of-plane spin relaxation behavior.

4 Lateral spin valves and Hanle precession in graphene/TMDC heterostructures

The concept behind lateral spin valves (LSV) dates back to 1985, when Johnson and Silsbee proposed a method[81] to induce a nonequilibrium spin density in a nonmagnetic material by injecting a spin-polarized charge current. The typical nonlocal LSV experiment is sketched in Fig. 3, where two ferromagnets F_1 and F_2 are placed on top of a nonmagnetic metal and a spin-polarized current I_0 is forced to flow from the injector at F_1 to the left of the device. This leads to the formation of a spin density accumulation $\boldsymbol{n}_s$ in the region below F_1, which points parallel to the magnetization direction. The electrically-induced spin density then propagates diffusively through the material and can be detected by F_2, allowing for the determination of n_s, λ_s, and τ_s.

In the presence of a magnetic field B, the dynamics of the spin density can be described by the Bloch-Torrey equations (BTE)

$$D_s \nabla^2 \boldsymbol{n}_s + \frac{\partial \boldsymbol{n}_s}{\partial t} = -\Omega \cdot \boldsymbol{n}_s + \omega_B \boldsymbol{n}_s \times \hat{\boldsymbol{e}}_B, \tag{9}$$

where ω_B is the Larmor precession frequency, D_s is the spin diffusion coefficient, $\hat{\boldsymbol{e}}_B$ is a unit vector pointing parallel to the magnetic field, and Ω is a matrix representing the spin relaxation rates. In the coordinate basis $\{\hat{\boldsymbol{e}}_x, \hat{\boldsymbol{e}}_\parallel, \hat{\boldsymbol{e}}_\perp\}$, where the unit vectors point in the propagation, magnetization, and out-of plane directions respectively, the relaxation rate matrix has the form

$$\Omega = \begin{bmatrix} 1/\tau_s^\parallel & 0 & 0 \\ 0 & 1/\tau_s^\parallel & 0 \\ 0 & 0 & 1/\tau_s^\perp \end{bmatrix}. \tag{10}$$

In the absence of magnetic field, the BTE equations are decoupled and the spin density parallel to the injector's magnetization has the simple exponential solution

$$n_s^\parallel(x) = \frac{PI_0}{2eD_s\sigma} \frac{\lambda_s^\parallel}{w} e^{-|x|/\lambda_s^\parallel}, \tag{11}$$

where P is the spin injection efficiency, w is the width of the channel, and σ is the conductivity. When the spin density arrives at the detector, it is transformed into a voltage that will depend on the relative orientation between the magnetization of F_1 and F_2. To eliminate background effects, the voltage is measured with the injector/detector magnetized in parallel (P) and antiparallel (AP)

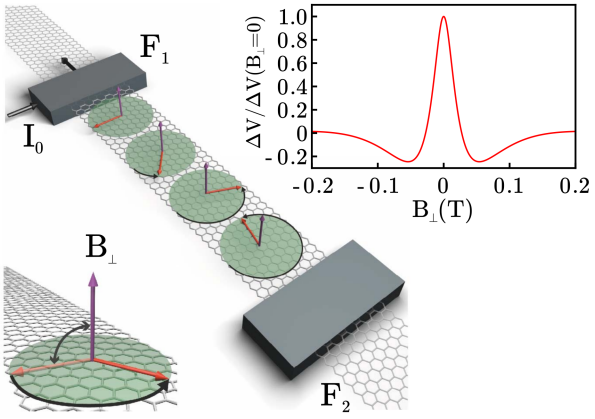

Fig. 3 Schematic of a LSV in the presence of a perpendicular magnetic field. At the injector a spin-polarized charge current is injected, leading to the formation of spin accumulation below F_1 which propagates diffusively through the channel. The out-of-plane magnetic field drives spin precession around the perpendicular axis, giving rise to dephasing and suppression of the non-local voltage. Courtesy of S. Valenzuela[61].

orientations. The voltage difference can be expressed as

$$\Delta V = PeD_s n_s^{\parallel}(L) = P^2 \frac{I_0}{\sigma}\frac{\lambda_S^{\parallel}}{w} e^{-L/\lambda_s^{\parallel}}, \tag{12}$$

where L is the distance between F_1 and F_2. This measurement thus provides a direct probe of the in-plane spin relaxation length $\lambda_s^{\parallel}$. In order to also extract the spin relaxation times, an external magnetic field must be applied, as discussed in the next sections.

4.1 Out-of-plane magnetic field

In the presence of a perpendicular magnetic field, the spin will precess in the plane of the material, as shown in Fig. 3. In this situation, the out-of-plane component of the spin density decouples from the BTE equations, leading to two coupled equations that depend on the in-plane relaxation time. Their solution yields

$$n_s^{\parallel}(L) = n_s^{\parallel}(L,0)\int_0^{\infty} P(L,t)\exp^{-t/\tau_s}\cos(\omega_B t)dt, \tag{13}$$

where

$$P(L,t) = \frac{1}{\sqrt{4\pi D_s t}} e^{-\frac{L^2}{4D_s t}} \tag{14}$$

denotes the probability that a spin reaches the detector at time t, and the integral over time captures all diffusive paths that reach the detector. The second term in the integral accounts for spin relaxation during this time, and the third term describes precession induced by the magnetic field.

Equation (13) can be solved analytically, yielding an expression for the nonlocal voltage that is quite similar to Eq. (12),

$$\Delta V = \mathrm{Re}\left\{P^2 \frac{I_0}{\sigma}\frac{\tilde{\lambda}_s^{\parallel}}{w} e^{-L/\tilde{\lambda}_s^{\parallel}}\right\}, \tag{15}$$

where $\tilde{\lambda}_s^{\parallel}$ is a complex renormalization of the spin relaxation length due to the effect of the magnetic field,

$$\tilde{\lambda}_s^{\parallel} = \frac{\lambda_s^{\parallel}}{\sqrt{1+i\omega_B\tau_s^{\parallel}}}. \tag{16}$$

The applied magnetic field can therefore modulate and completely suppress the spin signal, as shown in the inset of Fig. 3. Moreover, this modulation allows the extraction of the in-plane relaxation time $\tau_s^{\parallel}$. However, this measurement does not provide information about the out-of-plane component.

4.2 In-plane magnetic field

In order probe the out-of-plane spin relaxation, a magnetic field can be applied parallel to the propagation direction $\hat{\boldsymbol{e}}_{\boldsymbol{x}}$, which allows the spin to precess out of the graphene plane. For this case, the equation for n_s^x decouples from the others, leaving a system of two equations that this time involve $\tau_s^{\parallel}$ and $\tau_s^{\perp}$. These equations can be solved by rewriting the BTE in matrix form,

$$\begin{bmatrix} n_s^{\parallel}(x) \\ n_s^{\perp}(x) \end{bmatrix} = \begin{bmatrix} n_s^{\parallel}(0) \\ n_s^{\perp}(0) \end{bmatrix} e^{-x\Lambda^{-1}}, \tag{17}$$

where

$$\Lambda^{-2} = \left(\lambda_s^{\parallel}\right)^{-2}\begin{bmatrix} 1 & -\omega_B\tau_s^{\parallel} \\ \omega_B\tau_s^{\parallel} & 1/\zeta \end{bmatrix} \tag{18}$$

is the matrix generalization of λ_s^{-2}. The problem thus reduces to a computation of the matrix $\exp(-x\Lambda^{-1})$. The solution is too cumbersome to show here; instead we present the results for some typical experimental values in Fig. 4(a). When compared to the Hanle curve with out-of-plane magnetic field shown in Fig. 3, one can immediately see the impact of the spin lifetime anisotropy. At finite in-plane magnetic fields, the spin will experience a combination of the in-plane and out-of-plane spin relaxation times. For spin lifetime anisotropy $\zeta > 1$, the effective spin lifetime will be enhanced compared to the pure in-plane lifetime, leading to an enhanced nonlocal signal at finite magnetic fields. This can be clearly seen in Fig. 4(a), where the maximum of the nonlocal signal increases with increasing ζ, and is in contrast to Fig. 3, where the nonlocal signal is maximized at $B = 0$.

4.3 Oblique magnetic field

An alternative approach for measuring the spin lifetime anisotropy is to align the magnetic field perpendicular to the transport direction, in the $\hat{\boldsymbol{e}}_{\parallel} - \hat{\boldsymbol{e}}_{\perp}$ plane. In the limit of large magnetic field, the components of spin perpendicular to B will become completely dephased, and the detector will only measure the component parallel to the magnetic field, given by

$$n_s^B \equiv \boldsymbol{n}_s \cdot \hat{\boldsymbol{e}}_B = |\boldsymbol{n}_s|\cos\beta, \tag{19}$$

where β is the angle between the field and $\hat{\boldsymbol{e}}_{\parallel}$. At finite β, the effective spin relaxation length is a combination of the in-plane

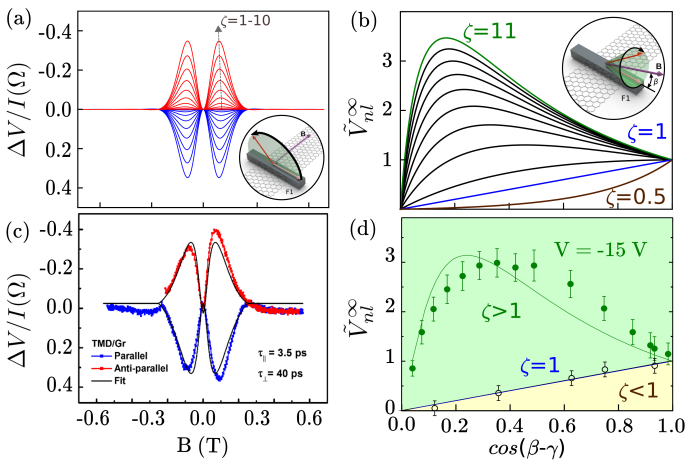

Fig. 4 (a) Theoretical nonlocal spin signal vs. in-plane magnetic field for different values of spin lifetime anisotropy. (b) Normalized high-field nonlocal voltage as a function of the oblique magnetic field angle β, for different anisotropy values. Curves in red, blue, and green highlight the cases $\zeta = 11$, 1, and $1/2$ respectively. (c) Experimental values of the nonlocal resistance modulated by an in-plane magnetic field, reproduced from Ref. 65. (d) Normalized high-field nonlocal voltage as a function of the oblique angle β for pristine graphene and graphene/WS_2, reproduced from Ref. 66. In both (c) and (d) there is a tenfold enhancement of the anisotropy compared to graphene on SiO_2 or hBN.

and out-of-plane spin relaxation[61,62],

$$\lambda_s^B = \lambda_s^{\parallel}\sqrt{(\cos^2\beta + \frac{1}{\zeta}\sin^2\beta)}. \tag{20}$$

Equations (19) and (20) enable the extraction of the spin anisotropy by measuring the nonequilibrium spin density as a function of β. Experimentally, the nonlocal voltage at large magnetic field is normalized by the value at $B = 0$, and has the form

$$\tilde{V}_{nl}^{\infty}(\beta,\zeta) = \frac{\lambda_s^{\parallel}}{\lambda_s^B}\exp\left(-\frac{L}{\lambda_s^{\parallel}}\left(\frac{\lambda_s^B}{\lambda_s^{\parallel}} - 1\right)\right)\cos^2\beta. \tag{21}$$

This expression reduces to $\cos^2\beta$ when the spin relaxation is isotropic. In Fig. 4(b), we show $\tilde{V}_{nl}^{\infty}(\beta,\zeta)$ as a function of $\cos^2\beta$ for different values of anisotropy. For $\zeta < 1$ ($\zeta > 1$), the curve falls below (above) the curve for $\zeta = 1$.

4.4 Hanle measurements in graphene/TMDC heterostructures

In the first experimental measurement of Hanle precession in these systems, the nonlocal spin signal of a LSV in a graphene/MoS_2 heterostructure was shown to be tunable with an electrical gate, exhibiting an on/off behavior that persisted up to 200 K[23]. A subsequent experiment reproduced these results at room temperature, also in graphene/MoS_2[25]. Figure 5(a) shows this on/off behavior for the room temperature measurements, with the spin relaxation time dropping to zero at positive gate voltages. Although it is tempting to associate this behavior with proximity-induced spin-orbit coupling, it is in fact a spin absorption effect. As shown in Fig. 5(b), the electronic structure of graphene/MoS_2 has its Fermi level close to the MoS_2 conduction band, meaning that a positive gate voltage will induce parallel spin conduction in both graphene and MoS_2. The latter, having SOC of the order of hundreds of meV[82], produces a much faster spin relaxation than in graphene and no spin signal will be detected. On the other hand, below this threshold voltage spins are only transported in graphene bands, where longer $\tau_s^{\parallel}$ and $\lambda_s^{\parallel}$ are expected, and a spin signal can be measured. This theory of spin absorption has also been supported by measurements of the Schottky barrier between graphene and MoS_2[25].

While the suppression of spin signal at positive gate voltages is attributable to spin absorption, the magnitude of $\tau_s^{\parallel}$ at negative gate voltages, with values less than 60 ps, suggests a proximity-induced SOC in the graphene layer. This is in contrast to graphene on SiO_2 or hBN, which typically has spin relaxation times of hundreds of ps to a few ns[11,12,15,44–53]. Comparable results were also observed in graphene/WS_2 heterostructures, where $\tau_s^{\parallel}$ was measured to be around 20 ps[83]. However, the spin lifetime in the "clean" region of these devices was only around 40 ps. Thus, while these low spin lifetimes are suggestive of enhanced SOC in graphene, they are not experimental proof of this effect. As discussed in Section 3.2, one of the consequences of the SOC induced in graphene by TMDCs is an unconventional large spin lifetime anisotropy[76]. Therefore, an experimental measurement of this phenomenon would provide strong evidence of proximity-induced SOC in graphene.

In two very recent experiments, a careful Hanle analysis was performed on graphene/$MoSe_2$ and graphene/WSe_2 at 75 K[65], and on graphene/WS_2 and graphene/MoS_2 at room temperature[66]. The first set of measurements was performed using the in-plane magnetic field technique described in Section 4.2, while the room temperature results were obtained using both this technique and oblique magnetic fields. In both experiments, the Hanle precession curves have shapes that are indicative of large spin lifetime anisotropy when the applied magnetic field allows the spins to rotate out of the graphene plane. Analysis of the measurements resulted in anisotropies of $\zeta > 10$ for all substrates and temperatures. This is shown in Fig. 4, where the modeled curves for the in-plane and the oblique-field Hanle measurements are shown in panels (a) and (b), respectively, while the the corresponding measurements are in panels (c) and (d).

In these measurements, the graphene/WSe_2 heterostructure shows a giant anisotropy of $\zeta \approx 40$, in contrast to $\zeta \approx 11$ in graphene/$MoSe_2$. This difference is reasonable considering that tungsten is a heavier element than molybdenum, and consequently it induces a larger valley-Zeeman SOC[74]. On the other hand, the measurements at room temperature of both graphene/WS_2 and graphene/MoS_2 exhibit $\zeta \approx 10$. One possible explanation for the lesser anisotropy of the WS_2 heterostructure could be increased intravalley scattering due to phonons at room temperature, although it is not clear why this would impact WS_2 more than MoS_2. Another possibility is the quality of the graphene/TMDC interface. Although graphene/WS_2 has theoretically the highest λ_{VZ}/λ_R, the distance between the graphene and the TMDC can significantly impact the induced SOC strength[21,64,74]. This could also explain some of the discrep-

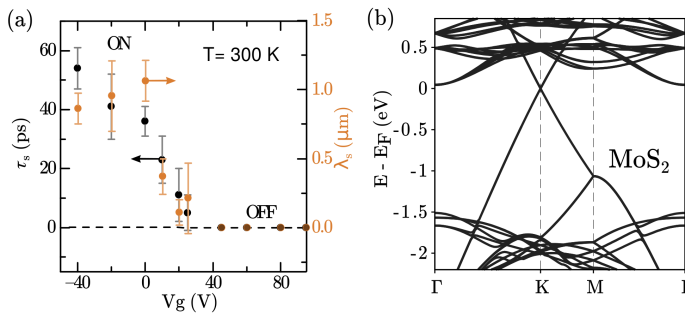

Fig. 5 (a) Spin relaxation times and lengths obtained for a graphene/MoS_2 heterostructure, reproduced from Ref. 25. (b) Band structure for graphene/MoS_2 reproduced from Ref. 74. For this heterostructure, the graphene Dirac cone lies close to the valence band of MoS_2, allowing for transport within its bulk bands for positive gate voltage. Given the strong SOC in the TMDC, the spin relaxes immediately after its absorption, leading to the switching behavior.

ancies between the measurements and the theoretical model[76], which predicts values of ζ ranging from 20 to 200. Nevertheless, unprecedented spin lifetime anisotropy is clearly seen at room temperature, which is a crucial condition for implementing such heterostructures in spintronic devices. In addition, the oblique field measurements in sulphur-based TMDCs at different gate voltages also showed an on/off behavior in the spin signal[66], in agreement with the aforementioned MoS_2-based devices. Meanwhile, this effect was not observed in selenium-based TMDCs, possibly due to their different band alignments[74].

Finally, the modulation of the spin lifetime has recently been measured in a double-gated graphene/WS_2 heterostructure[84]. The combination of a top and bottom gate allows one to maintain the Fermi level while tuning the electric field, which directly controls the Rashba SOC strength[74]. By doing so, a fourfold modulation of $\tau_s^{\parallel}$ was observed as well as indications that $\zeta < 1$ in the strong Rashba regime. Moreover, the spin relaxation mechanism is predicted to be DP. Hence, these results not only support the microscopic theory of spin relaxation presented above, but also demonstrate an all-electric route to tune proximity effects in graphene.

In conclusion, the Hanle experiments demonstrate that one can tune both the proximity effects and the spin transport in graphene by choosing the appropriate TMDC substrate. It is clear that strong SOC is induced in graphene no matter which TMDC is utilized, but also that the valley-Zeman SOC and intervalley scattering play an important role in these systems[76].

5 Weak Antilocalization in graphene/TMDC heterostructures

In addition to directly measuring the spin signal, as described in Section 4, it is also possible to use charge transport measurements to glean information about the spin relaxation mechanisms in a material. This is done by measuring the weak localization (WL) and weak antilocalization phenomena, which are quantum corrections to the classical conductivity and are summarized in Fig. 6. In a diffusive system, charge scattering leads to a randomized path as an electron passes through a material. Some of these paths involve closed loops that result in backscattering, which can be traversed in either direction, as shown in Fig. 6(a). Owing to the wave nature of electrons, these two opposite loops can constructively interfere with one another, increasing the weight of this backscattering path and reducing the overall conductivity compared to the classical case[85]. This is weak localization, and is illustrated in Fig. 6(b). In the presence of spin-orbit coupling, the phase between these opposite loops switches sign, leading to destructive interference. This reduces the weight of the backscattering loop and increases the conductivity relative to the classical value[86]. This is the process known as WAL, and is shown in Fig. 6(c). By applying a magnetic field, one can tune the phase accumulated along each diffusive path, and thus alter the interference properties of the backscattering loops. This will modulate the conductivity, and its precise dependence on magnetic field can be used to infer the strength of the various charge and spin relaxation mechanisms in the measured system[86,87].

5.1 WAL Theory

A comprehensive description of WAL in graphene was developed by McCann and Fal'ko[73], where they derived the quantum correction to the conductivity as

$$\begin{aligned}\Delta\sigma(B) &\equiv \sigma(B) - \sigma(0) \\ &= -\frac{e^2}{2\pi h} \sum_{j,l=0,x,y,z} c_j c_l F\left(\frac{\tau_B^{-1}}{\tau_\phi^{-1} + \Gamma_j^l}\right),\end{aligned} \tag{22}$$

where $F(z) = \ln(z) + \Psi(1/2 + 1/z)$, Ψ is the digamma function, $c_0 = 1$, $c_x = c_y = c_z = -1$, $\tau_B^{-1} = 4DeB/\hbar$, D is the diffusion coefficient, B is the external magnetic field perpendicular to the graphene plane, and τ_ϕ is the inelastic dephasing time. The Γ_j^l describe the various relaxation rates in the system that arise from symmetry breaking, and include both spin and charge relaxation. For interference effects to occur, the electrons must maintain phase coherence around the scattering loops; in general the relation $\tau_\phi^{-1} < \Gamma_j^l$ satisfies this condition.

Eq. (22) contains a total of 16 terms, but is typically simplified by assuming that the intervalley scattering time, τ_{iv}, is much smaller than the spin lifetimes. All terms containing τ_{iv} can then be neglected, leaving

$$\begin{aligned}\Delta\sigma(B) = -\frac{e^2}{2\pi h}\Bigg[&F\left(\frac{\tau_B^{-1}}{\tau_\phi^{-1}}\right) - F\left(\frac{\tau_B^{-1}}{\tau_\phi^{-1} + 2\tau_{asy}^{-1}}\right) \\ &- 2F\left(\frac{\tau_B^{-1}}{\tau_\phi^{-1} + \tau_{asy}^{-1} + \tau_{sym}^{-1}}\right)\Bigg].\end{aligned} \tag{23}$$

Here, τ_{asy} is the spin relaxation time arising from symmetry breaking perpendicular to the graphene plane, typically associated with Rashba SOC[88]. Meanwhile, τ_{sym} is the spin relaxation time associated with SOC that maintains perpendicular symmetry, which is usually ascribed to intrinsic, or Kane-Mele[31], SOC. The total spin relaxation time is then defined as $\tau_{so}^{-1} \equiv \tau_{asy}^{-1} + \tau_{sym}^{-1}$.

Figures 6(d) and (e) show examples of the magnetoconductiv-

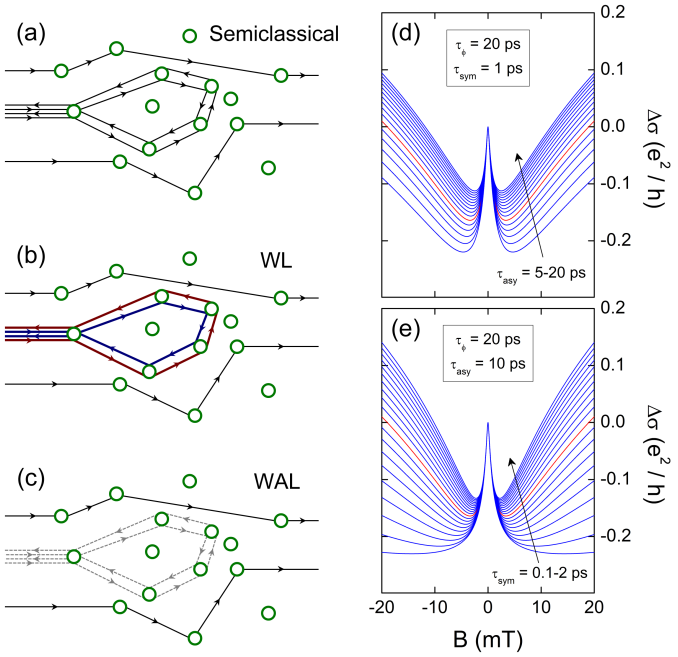

Fig. 6 Summary of WAL in diffusive materials. Panel (a) depicts charge transport in the semiclassical regime, including a pair of backscattering loops. Panels (b) and (c) illustrate the case in the WL and WAL regimes, where the backscattering loops constructively or destructively interfere, respectively. Panels (d) and (e) show magnetoconductance curves using typical relaxation times for graphene/TMDC heterostructures.

ity and how it depends on τ_{asy} and τ_{sym}. The red curves show the case for a baseline set of parameters that are typical of those measured in graphene/TMDC heterostructures: $\tau_\phi = 20$ ps, $\tau_{asy} = 10$ ps, and $\tau_{sym} = 1$ ps. In Fig. 6(d) we vary τ_{asy} between 5 and 20 ps, and in this range one can see that the primary effect is to scale the height of the central WAL peak, with smaller τ_{asy} yielding a larger peak. In Fig. 6(e) we vary τ_{sym} between 0.1 and 2 ps, and find that its primary role is to adjust the slope of $\Delta\sigma$ at higher magnetic fields, with a flat profile indicative of a small τ_{sym}.

5.2 Measurements of WAL in graphene/TMDC heterostructures

The first measurements of WAL in a graphene/TMDC heterostructure were made in graphene on a WS_2 substrate[21]. After averaging out conductance fluctuations, the magnetoconductance curves exhibited large WAL peaks around $B = 0$, indicating strong SOC induced in graphene by the WS_2 substrate. Fits to Eq. (23) yielded $\tau_{so} \approx 2.5 - 5$ ps, and τ_{asy} was estimated to be approximately 3× larger. Although the role of valley-Zeeman SOC was not considered, the authors noted a strong correlation between τ_{so} and τ_{iv}. This was attributed to spatial fluctuations of the spin-orbit coupling strength, which were posited to simultaneously cause intervalley scattering and relax the spin.

The next reported measurement[64] also considered a graphene/WS_2 device. In the WAL analysis, the impact of intrinsic SOC on τ_{sym} was assumed to be negligible, as was the valley-Zeeman SOC. This left τ_ϕ and τ_{asy} as the only fitting parameters in Eq. (23), from which $\tau_{asy} \approx 5$ ps was extracted. This relaxation time was found to scale inversely with the momentum scattering time, and could also be tuned by ~10% in either direction with a vertical electrical field. Both of these observations are suggestive of the DP mechanism of spin relaxation induced by Rashba SOC, with an estimated Rashba strength of $\lambda_R \approx 0.4$ meV. A follow-up work by the same group[26] found similar results for graphene interfaced with WSe_2 and MoS_2. Using the same analysis they found $\tau_{so} \approx 2 - 10$ ps, which scaled inversely with τ_p, giving $\lambda_R \approx 1.5\,(0.9)$ meV for graphene interfaced with WSe_2 (MoS_2).

An independent set of measurements of graphene/WSe_2 also concluded that spin relaxation was dominated by the traditional DP mechanism, but considered both τ_{asy} and τ_{so} in the WAL fits[78]. These fits yielded $\tau_{asy} = 1.7 - 4.5$ ps and $\tau_{so} = 0.9 - 1.5$ ps, and by examining the relationship between τ_{so} and τ_p, a Rashba spin-orbit strength of $\lambda_R \approx 0.7 - 1$ meV was extracted.

Meanwhile, a comprehensive set of WAL measurements demonstrated the importance of eliminating classical effects from the magnetoconductance[24]. At high temperatures the dephasing time τ_ϕ becomes very short, washing out interference effects, and any dependence of the conductivity on the magnetic field can be considered to arise from classical effects. In these measurements, subtracting the high-temperature magnetoconductivity curves from the low-temperature curves resulted in a sharp WAL peak and little to no upturn of $\Delta\sigma$ at higher fields; see Figs. 7(a) and (b) for an example. As shown in Fig. 6(e), this flat profile of $\Delta\sigma$ is indicative of very fast spin relaxation. Indeed, fits to WAL theory yield upper bounds of $\tau_{so} \leq 0.1 - 0.4$ ps. As shown in Fig. 7(c), this behavior is found over many devices, including different TMDCs (MoS_2, WS_2, and WSe_2) and a wide range of mobilities ($3000 - 110\,000$ cm^2/V·s). Although small values of τ_{so} were reported, the individual values of τ_{asy} and τ_{sym} were not. Finally, by analyzing Shubnikov-de Haas oscillations in bilayer graphene/WSe_2 devices, the Rashba SOC strength was estimated to be $\lambda_R \approx 10 - 15$ meV, which is one order of magnitude larger than what was found in other measurements or in *ab initio* simulations[24,64,74].

While all of these measurements demonstrate significant proximity-induced SOC in graphene, the analyses do not consider the impact of valley-Zeeman SOC. As predicted theoretically[76], and confirmed by Hanle measurements[65,66], valley-Zeeman SOC is responsible for fast relaxation of the in-plane spins and a resultant giant spin lifetime anisotropy. As shown very recently, a careful analysis of WAL measurements can reveal this behavior[68]. According to the theory of McCann and Fal'ko, τ_{sym} is determined by both intrinsic and valley-Zeeman SOC, while τ_{asy} is dominated by Rashba SOC[73]. As discussed in Refs. 26,64,68,78, the contribution of intrinsic SOC is negligible, leaving valley-Zeeman SOC as the only contributor to τ_{sym}. Connecting to the theory presented in Section 3.2, Eq. (7), one can then assign $\tau_{asy} = 2\tau_s^\perp$ and $\tau_{so} = \tau_s^\parallel$, which allows a determination of both λ_R and λ_{VZ}. Additionally, the spin lifetime anisotropy can be estimated as $\zeta = \tau_{asy}/2\tau_{sym}$. In recent measurements of graphene/WSe_2 devices[68], this analysis resulted in $\lambda_R \approx 0.35$ meV, $\lambda_{VZ} \approx 0.2 - 2$ meV, and $\zeta \approx 20$. These results match well with DFT calcula-

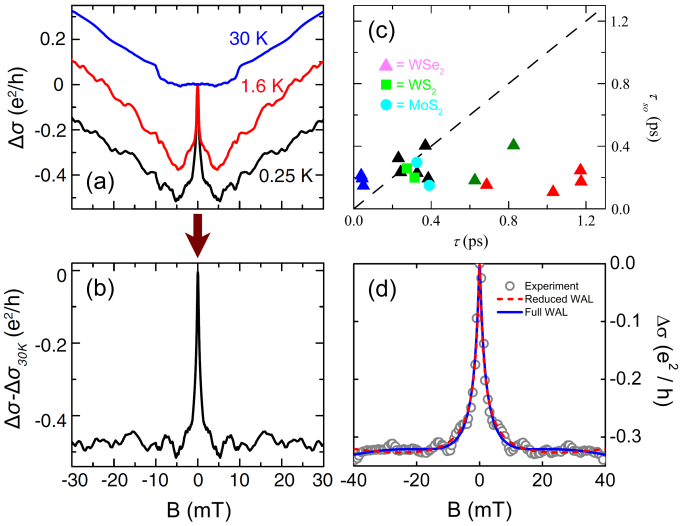

Fig. 7 (a) Temperature-dependent evolution of the magnetoconductance in a graphene/WS_2 heterostructure. Subtracting the high-temperature classical signal gives the normalized magnetoconductivity shown in (b). Panel (c) shows a summary of WAL measurements made using this background subtraction, yielding a uniform spin-orbit time across a wide range of devices and TMDCs. Panels (a)-(c) are reproduced from Ref. 24. (d) Fits to magnetoconductance using the full and the reduced WAL formulas of Eqs. (22) and (23), with experimental data extracted from Ref. 67.

tions[63,64,74], spin relaxation theory[76], and the Hanle measurements of spin lifetime anisotropy[65,66] and thus highlight the importance of considering the valley-Zeeman SOC when studying quantum transport in these systems.

5.3 WAL analysis in the strong-SOC regime

As mentioned in Section 5.1, Eq. (23) was derived assuming the strong-scattering/weak-SOC regime, i.e., in the limit $\tau_{iv} \ll \tau_{so}$. However, owing to graphene's exceptional charge transport properties and the strong SOC induced by the TMDC, this condition can be violated in graphene/TMDC heterostructures. Indeed, this appears to be the case in at least one of the aforementioned WAL measurements[24], where $\tau_{so} \approx \tau_p$. This then raises the question, are the fits obtained from Eq. (23) reasonable, or is a more general fit using Eq. (22) required?

The full WAL equation includes two extra relaxation times, τ_{iv} and τ_z, the latter of which is an intravalley scattering time related to fluctuations in the onsite energy of the graphene A/B sublattices, and fluctuations in the nearest-neighbor hopping. With a total of five parameters, finding a unique fit is much more difficult in this regime, and a measurement that captures the tails of the magnetoconductance at higher magnetic fields is crucial. Therefore, we consider a very recent measurement of magnetoconductivity out to ±40 mT in a graphene/WS_2 system[67], displayed as the open circles in Fig. 7(d). The mobility of this sample is $\mu = 12\,000$ cm^2/V·s, giving $\tau_p \approx 0.1$ ps.

The dashed red line in Fig. 7(d) shows the fit using the reduced WAL theory of Eq. (23), which yields $\tau_{asy} = 3.6$ ps and $\tau_{sym} = 0.05$ ps. Because $\tau_{sym} < \tau_p$, Eq. (23) is clearly beyond its range of validity. The solid blue line shows the fit to the full WAL formula. In this fit, there remains a fair amount of flexibility in the values of τ_{iv} and τ_z, all of which give nearly identical magnetoconductance curves. By varying τ_{iv} and τ_z in the ranges $\tau_{iv} \in [2, 15]\tau_p$ and $\tau_z \in [0.5, 2]\tau_p$, we find $\tau_{asy} = 1.6 - 2.5$ ps and $\tau_{sym} = 0.3 - 0.5$ ps. This analysis shows that when the conditions of Eq. (23) are violated, considering the full WAL theory can have a considerable impact on the estimate of τ_{sym}, increasing it by a factor of 6 – 10 in this particular case. Looking forward, an independent measurement of τ_{iv} would make for an easier fit to Eq. (22).

6 Spin Hall Effect

The spin Hall effect is a phenomenon by which an electric current produces a transverse spin current as a result of spin-orbit coupling[32]. The spin Hall effect is thus a purely electrical source of spin current, which makes it an important topic for spintronics. Depending on its origin, the spin Hall effect is classified as either extrinsic or intrinsic. The extrinsic spin Hall effect is driven by scattering with strong SOC impurities, which allows for anisotropic spin-dependent scattering. The intrinsic spin Hall effect, on the other hand, is generated by the homogeneous SOC field present in the electronic structure of the material. In Section 3.1 we showed that TMDCs induce nontrivial SOC in graphene, with valley-Zeeman being the dominant term. We will see in this section that this SOC field may also generate a relatively large spin Hall effect close to the charge neutrality point[89]. Moreover, guided by the theoretical framework of the previous sections, we will discuss the conditions needed to measure the intrinsic SHE in graphene/TMDC systems. Finally, it is important to note that the intrinsic mechanism may not be the only source of spin Hall effect, as chalcogenide vacancies could produce the extrinsic SHE[18]. However, given that up to now there is no clear evidence of this effect, we will focus on the intrinsic SHE.

6.1 Topology and spin Hall effect in graphene/TMDCs

In the previous sections we have shown that treating the SOC as a spin-dependent magnetic field is sufficient to quantitatively explain the various experimental and numerical results. Similarly, one may argue that a spin-dependent magnetic field should also affect the orbital motion of electrons, giving rise to a spin-dependent Hall effect. This is indeed the case, although the connection between the spin Hall effect and the spin-orbit coupling is not straightforward.

To visualize this, consider a system in equilibrium with no net spin or charge current. Under such a situation the spins are aligned with the spin-dependent magnetic field, as illustrated in Fig. 1. After the application of an external electric field $\boldsymbol{E}$, the system undergoes two changes: first, the Fermi surface is shifted, leading to an asymmetric population of momentum in the direction of $\boldsymbol{E}$. Second, the eigenfunctions $\phi_n(\boldsymbol{k})$ of the system are modified, and with them the expectation values of all observables. For example, the velocity operator takes the form

$$\boldsymbol{v}_n(\boldsymbol{k}) = \boldsymbol{\nabla}\varepsilon_n(\boldsymbol{k}) - \frac{e}{\hbar}\boldsymbol{E} \times \boldsymbol{\Omega}_n, \tag{24}$$

where n is the band index, $\boldsymbol{k}$ is the electron momentum, $\varepsilon_n(\boldsymbol{k})$ is

the dispersion relation, and

$$\boldsymbol{\Omega}_n(\boldsymbol{k}) = i\,\boldsymbol{\nabla} \times \left[\, \phi_n^*(\boldsymbol{k}) \boldsymbol{\nabla} \phi_n(\boldsymbol{k}) \,\right] \tag{25}$$

is the Berry curvature (BC) [32,90]. Equation (24) shows that under the action of an electrical field, the velocity acquires a contribution directly related to the eigenfunctions, which is the origin of the different Hall effects [28,91].

In spintronic devices, the figure of merit for the spin Hall effect is the spin Hall angle

$$\gamma_{\mathrm{sH}} \equiv \frac{\sigma_{xy}^z}{\sigma_{xx}}, \tag{26}$$

where σ_{xx} is the longitudinal charge conductivity and σ_{xy}^z is the spin Hall conductivity defined through the relation $j_{s,\beta}^z = \sigma_{\alpha\beta}^z E_\alpha$, where $j_{s,\beta}^z$ is the β component of the spin current polarized in the out-of-plane direction [28]. The spin current can be determined microscopically as the the expectation value of the spin current operator $\hat{\jmath}_\beta^z$, which for a system out of equilibrium is computed as [28,32,92]

$$j_{s,\beta}^z = \langle \hat{\jmath}_\beta^z \rangle \equiv \mathrm{Tr}\left[\hat{\jmath}_\beta^z \hat{\rho}_{\mathrm{neq}}\right], \tag{27}$$

where

$$\hat{\rho}_{\mathrm{neq}} = i\hbar e E_\alpha \int d\varepsilon f(\varepsilon) \left(\frac{dG^+(\varepsilon)}{d\varepsilon} \hat{v}_\alpha \delta(\varepsilon - H) - \mathrm{h.c.} \right), \tag{28}$$

is the nonequilibrium density matrix due to electric field E_α, with $\hat{v}_\alpha$ the α component of the velocity operator, $f(\varepsilon)$ the Fermi-Dirac distribution function, and G^+ the retarded single-particle Green's function. The spin current operator is given by

$$\hat{\jmath}_\beta^z \equiv -\frac{e}{2\hbar\Omega}\{\sigma_z, \hat{v}_\beta\}, \tag{29}$$

with the curly brackets representing the anticommutator and Ω the volume of the sample. Given that the spin Hall conductivity is proportional to the tranverse current, one could expect σ_{xy}^z to have some relation with the Berry curvature. Indeed, as demonstrated by Thouless *et al.* for the quantum Hall effect [91], and later extended to spin, the trace in Eq. (27) is proportional to the Berry curvature, but only for pristine systems [32,70,92].

In Fig. 8 we show the pristine spin Hall conductivity for different graphene/TMDC heterostructures, computed in Ref. 89. This quantity can be used to measure the potential of a material for generating transverse spin currents [30], and as such, WS_2 stands out as the most promising TMDC. As shown in the inset, the valley-Zeeman SOC only leads to spin Hall conductivity when combined with Rashba and/or intrinsic SOC.

6.2 The role of disorder

A nonzero Berry curvature is a necessary but not sufficient condition for the existence of the intrinsic SHE. An example of this is the suppression by disorder of the universal spin Hall conductivity in 2DEGs with Rashba SOC [32]. In fact, for any k-linear SOC there is no SHE in the diffusive regime as a consequence of a covariant conservation law for spin currents [93]. A recent extension of this theory to diffusive Dirac systems led to the same conclusion [94], an absence of intrinsic SHE in graphene with Rashba SOC. However,

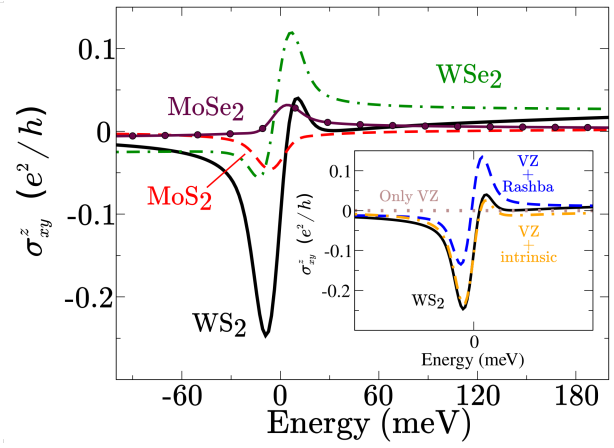

Fig. 8 Spin Hall conductivity for pristine graphene on different TMDCs. In the inset we show the effect of different SOC combinations on the spin Hall conductivity of WS_2. Data adapted from Ref. 89.

the presence of other SOC terms could allow for a breaking of the covariant law and a restoration of intrinsic SHE, even in the presence of disorder.

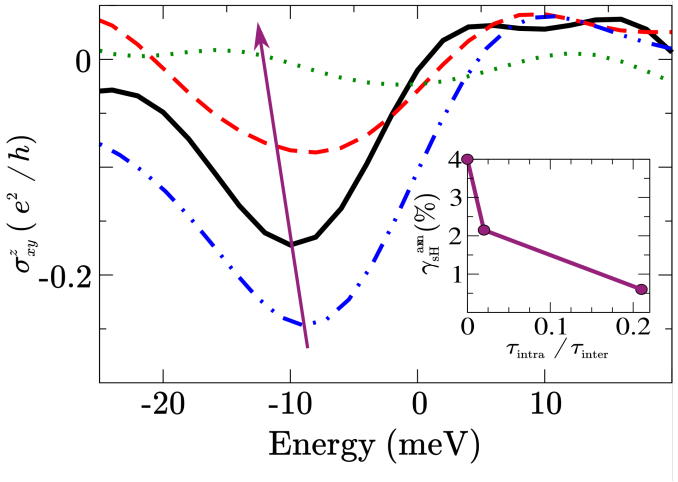

Fig. 9 Spin Hall conductivity of graphene/WS_2 for weak (solid black line), intermediate (dashed red line) and strong (dotted green line) intervalley scattering, with the pristine spin Hall conductivity (dot-dashed blue line) shown as a reference. The inset shows the scaling of the spin Hall angle with intervalley scattering strength. Data adapted from Ref. 89.

In previous sections, valley-Zeeman SOC and intervalley scattering were shown to play a central role in WAL and spin relaxation, and for the spin Hall effect the situation is no different. Because of time reversal symmetry, the Berry curvature has opposite sign in opposite valleys. Thus, in the presence of strong intervalley scattering the Berry curvature will average to zero, leading to a noticeable suppression of the spin Hall conductivity [89]. This can be seen in Fig. 9, where the spin Hall conductivity and spin Hall angle are computed using Eq. (27) for disorder profiles with similar mobilities but very different intervalley scattering rates. For weak intervalley scattering, the SHE is slightly reduced compared to the pristine case, but remains considerable. However, for

strong intervalley scattering the SHE is almost completely suppressed. This information is key for the design of experiments aiming to observe the SHE in graphene/TMDC systems, because structural defects and grain boundaries cause intervalley scattering and are usually found in large-area graphene[95], thus restricting the observation to exfoliated samples.

6.3 Experimental measurement of the SHE

Over the past several years, evidence of the spin Hall effect has been reported in graphene decorated with various adatoms[17,20,96], and in graphene/TMDC heterostructures[18]. All these measurements utilized a purely electrical experiment proposed by Abanin *et al*[97]. However, this proposal was developed for measuring a nonlocal signal originating from the extrinsic spin Hall effect, and it is not clear that the same approach can be used for the intrinsic SHE. To measure the intrinsic SHE, one needs to create and transport spin currents in a material with large SOC, but in such materials coherent spin precession can dephase and suppress the signal at the detector.

Given that SOC in pristine graphene is very small, one way to avoid such a situation is to place the TMDC only at the detection or injection region, as represented schematically in Fig. 10 and initially explored in Ref. 98 for platinum. Because the spin relaxes isotropically in pristine graphene, modulation due to a magnetic field can be described by the standard Hanle theory in Eq. (15) with the substitutions $P^2 \to \gamma_{\rm sH} P$ and $\mathrm{Re}\{...\} \to \mathrm{Im}\{...\}$. The inset of Fig. 10 shows the expected Hanle modulation with a magnetic field applied in the propagation direction. Using typical experimental parameters[66], a modulation of 2 μV is obtained, which is within the experimentally measurable range.

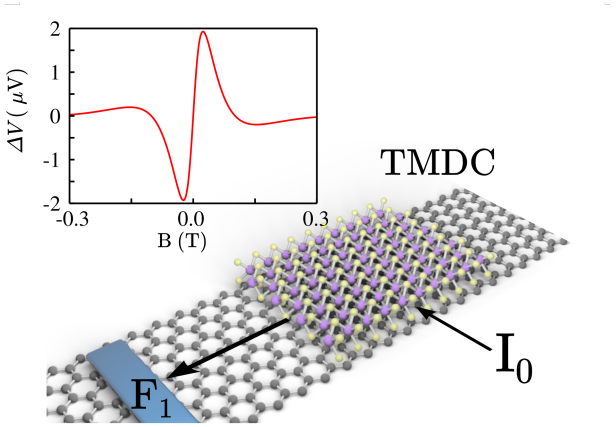

Fig. 10 Proposed setup for measuring the intrinsic SHE. A current is passed through the graphene/TMDC heterostructure, generating an out-of-plane spin current via the spin Hall effect. The inset shows the expected modulation of the nonlocal signal by an in-plane magnetic field.

6.4 Rashba-Edelestein effect

So far we have only considered the possibility of using the SHE to generate spin currents. Recently, it was shown that the inverse galvanic effect, also called the Rashba-Edelestein effect or current-induced spin polarization (CISP), can also be used for this purpose by generating nonequilibrium spin densities[99–103]. A simplified picture of CISP can be understood as follows: when an external electric field accelerates the electrons in a material, the spin-dependent magnetic field will rotate due to the change in the electron momentum. At steady state, the electrons will be aligned with the new rotated SOC field, leading to a nonequilibrium spin density. The existence of a steady state relies on scattering-induced damping of the spin precession, and thus care should be taken when considering the clean limit. Nonetheless, this limit can help to gain insight into the relative magnitudes of the CISP effect, and will serve as a baseline for future studies with disorder. In pure Rashba systems, the nonequillibrium spin density is perpendicular to the propagation and out-of-plane directions, and therefore the CISP will generate a contribution to $n_s^{\parallel}$ given by[104,105]

$$\delta n_s^{\parallel} = \frac{1}{3\pi} \frac{eE_x}{\eta_\phi v_F} \frac{\lambda_{\rm R}}{\hbar}, \tag{30}$$

where η_ϕ is an inelastic broadening, v_F is the Fermi velocity, and λ_R is the Rashba strength. Using $\lambda_R = 0.36$ meV for graphene/WS_2, $\eta = 2$ meV, and a typical electric field of $E_x = 1$ V/μm resuts in a nonequilibrium spin density of 0.5×10^8 cm^{-2}. This value is two orders of magnitude smaller than the nonequilibrium spin density created in typical spin injection experiments or in large-SOC metals[106], indicating that Rashba SOC by itself is not an efficient generator of nonequilibrium spin density.

In Fig. 11 we show the nonequilibrium spin density for graphene/TMDC heterostructures, computed using Eq. (27) with the replacement $j_\beta^z \to \sigma_y$. We also show the calculation for the pure Rashba system using the graphene/WS_2 Rashba parameter, with the simulation nicely reproducing the analytical prediction. However, despite having the same Rashba field, the nonequilibrium spin density for the full graphene/WS_2 model is one order of magnitude bigger, which comes from the combination of Rashba and valley-Zeeman SOC. Similar values are obtained for the other heterostructures, which places them, in terms of the CISP effect, next to other strong-SOC metals. While this result is a remarkable start, it should be taken with a grain of salt because disorder may greatly modify the overall effect.

7 Conclusions

In this review, we presented an introduction to the theory of spin-orbit effects induced in graphene by TMDCs, and their connection to measurements of Hanle precession, weak antilocalization, and the spin Hall effect. The common thread running through all of these topics is the presence of valley-Zeeman spin-orbit coupling, which significantly alters the behavior of spin transport in these systems by tying the in-plane spin dynamics to intervalley scattering processes. This leads to a giant anisotropy in the spin relaxation, with in-plane spins relaxing much faster than out-of-plane spins. As shown in Section 4, this anisotropy can be determined experimentally with variations on the traditional Hanle measurement. The valley-Zeeman SOC also plays an important role in weak antilocalization, as it appears to be responsible for the very short symmetric spin-orbit times that are extracted from magnetoconductivity measurements.

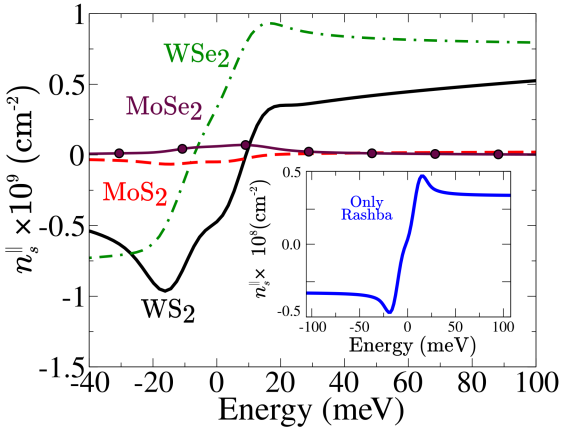

Fig. 11 Nonequilibrium spin density induced by an electric field of 1V/μm for different graphene/TMDC heterostructures, computed with the Kubo-Bastin formula. In the inset we show the case with only the Rashba parameter of WS_2.

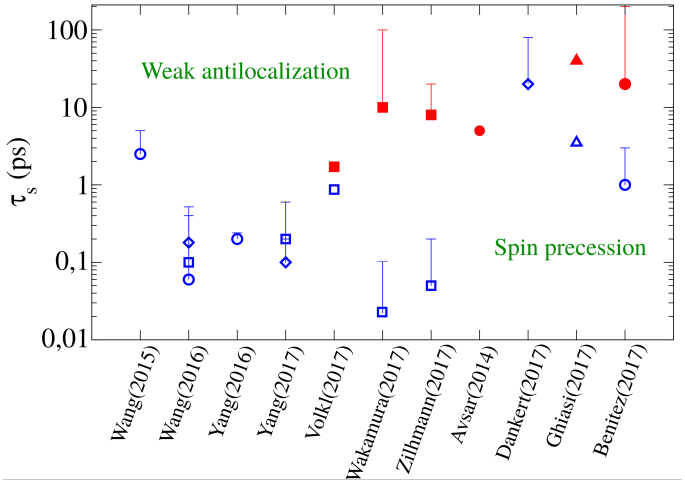

Fig. 12 Summary of the in-plane (open blue symbols) and out-of-plane (filled red symbols) spin relaxation times for different graphene/TMDC heterostructures, extracted from WAL and Hanle measurements. Squares, circles, diamonds, and triangles correspond to graphene interfaced with WS_2, WSe_2, MoS_2, and $MoSe_2$, respectively.The error bars denotes the variation over different momentum relaxation times.

In Fig. 12 we present a summary of all the experimental measurements of spin lifetime to date. The measurements reveal three main trends. First, the symmetric spin lifetimes derived from weak antilocalization and the Hanle in-plane spin lifetimes usually differ by an order of magnitude, which is something our theory currently does not capture, and which calls for further theoretical development as well as a measurement of both quantities within the same sample. Second, the spin lifetime anisotropy can vary from tens to hundreds in different experiments; this is not surprising given that different devices exhibit different disorder and interface quality, which would impact the intervalley scattering rates and SOC strength, respectively. Third, the spin lifetime of graphene is strongly suppressed, which, in combination with the giant spin lifetime anisotropy, is fundamental evidence of proximity-induced spin-orbit coupling.

Finally, our calculations have indicated that valley-Zeeman SOC can significantly enhance the intrinsic spin Hall effect in graphene. However, this effect is destroyed by intervalley scattering, meaning that it should only be measurable in systems without a sharp WAL signature and no spin lifetime anisotropy.

It is important to note that all our analyses have been performed considering scalar impurities and uniform SOC fields. However, there are experimental results suggesting that the SHE in graphene/TMDC heterostructures may also originate from chalcogenide vacancies [18]. These vacancies may constitute a kind of short-range disorder leading to strong intervalley scattering, thus suppressing the intrinsic SHE. However, they also possess a strong local SOC field which could then produce the extrinsic spin Hall effect. Therefore, by carefully tuning the concentration of vacancies, one could observe a transition from intrinsic to extrinsic spin Hall effect. If their local SOC is of the valley-Zeeman type, they could also be responsible for the anisotropy seen in the Hanle experiments, as well as the small symmetric spin-orbit times extracted from measurements of weak antilocalization. In the reduced WAL analysis of Eq. (23), the spin relaxation rates arising from uniform and nonuniform SOC are lumped together in both τ_{sym}^{-1} and τ_{asy}^{-1}, but considering the full WAL formula may allow one to separate these terms.

Finally, we would like to emphasize that such proximity-induced spin-orbit effects are not limited to TMDCs. In reality, these features are a consequence of broken symmetries in graphene [77], and any honeycomb substrate with broken sublattice symmetry should have a similar impact. In fact, it has recently been predicted that graphene on a topological insulator (TI) possesses very similar features [107], opening the door to a possibly rich interplay between graphene with proximity-induced SOC and TI surface states.

Acknowledgement

ICN2 is supported by the Severo Ochoa program from Spanish MINECO (Grant No. SEV-2013-0295) and funded by the CERCA Programme / Generalitat de Catalunya. The authors acknowledge the Spanish Ministry of Economy and Competitiveness and the European Regional Development Fund (Project No. FIS2015-67767-P MINECO/FEDER), the Secretaría de Universidades e Investigación del Departamento de Economía y Conocimiento de la Generalidad de Catalunya (2014 SGR 58), PRACE and the Barcelona Supercomputing Center (Project No. 2015133194), and the European Union Seventh Framework Programme under Grant Agreement No. 696656 Graphene Flagship.

Conflict of interest

There are no conflicts to declare.

References

1 A. C. Ferrari, F. Bonaccorso, V. Fal'ko, K. S. Novoselov, S. Roche, P. Bøggild, S. Borini, F. H. L. Koppens, V. Palermo, N. Pugno, J. A. Garrido, R. Sordan, A. Bianco, L. Ballerini, M. Prato, E. Lidorikis, J. Kivioja, C. Marinelli, T. Ryhänen, A. Morpurgo, J. N. Coleman, V. Nicolosi, L. Colombo, A. Fert, M. Garcia-Hernandez, A. Bachtold, G. F. Schnei-

der, F. Guinea, C. Dekker, M. Barbone, Z. Sun, C. Galiotis, A. N. Grigorenko, G. Konstantatos, A. Kis, M. Katsnelson, L. Vandersypen, A. Loiseau, V. Morandi, D. Neumaier, E. Treossi, V. Pellegrini, M. Polini, A. Tredicucci, G. M. Williams, B. Hee Hong, J.-H. Ahn, J. Min Kim, H. Zirath, B. J. van Wees, H. van der Zant, L. Occhipinti, A. Di Matteo, I. A. Kinloch, T. Seyller, E. Quesnel, X. Feng, K. Teo, N. Rupesinghe, P. Hakonen, S. R. T. Neil, Q. Tannock, T. Löfwander and J. Kinaret, *Nanoscale*, 2015, **7**, 4598–4810.

2 K. I. Bolotin, K. J. Sikes, Z. Jiang, M. Klima, G. Fudenberg, J. Hone, P. Kim and H. L. Stormer, *Solid State Commun.*, 2008, **146**, 351–355.

3 L. Banszerus, M. Schmitz, S. Engels, J. Dauber, M. Oellers, F. Haupt, K. Watanabe, T. Taniguchi, B. Beschoten and C. Stampfer, *Sci. Adv.*, 2015, **1**, e1500222—-e1500222.

4 L. Banszerus, M. Schmitz, S. Engels, M. Goldsche, K. Watanabe, T. Taniguchi, B. Beschoten and C. Stampfer, *Nano Lett.*, 2016, **16**, 1387–1391.

5 H. Min, J. E. Hill, N. A. Sinitsyn, B. R. Sahu, L. Kleinman and A. H. MacDonald, *Phys. Rev. B - Condens. Matter Mater. Phys.*, 2006, **74**, 165310.

6 D. Huertas-Hernando, F. Guinea and A. Brataas, *Phys. Rev. B - Condens. Matter Mater. Phys.*, 2006, **74**, 155426.

7 M. Gmitra, S. Konschuh, C. Ertler, C. Ambrosch-Draxl and J. Fabian, *Phys. Rev. B - Condens. Matter Mater. Phys.*, 2009, **80**, 235431.

8 S. Konschuh, M. Gmitra and J. Fabian, *Phys. Rev. B - Condens. Matter Mater. Phys.*, 2010, **82**, 245412.

9 M. Wojtaszek, I. J. Vera-Marun, E. Whiteway, M. Hilke and B. J. van Wees, *Phys. Rev. B - Condens. Matter Mater. Phys.*, 2014, **89**, 035417.

10 W. Han, R. K. Kawakami, M. Gmitra and J. Fabian, *Nat. Nanotechnol.*, 2014, **9**, 794–807.

11 M. H. D. Guimarães, A. Veligura, P. J. Zomer, T. Maassen, I. J. Vera-Marun, N. Tombros and B. J. van Wees, *Nano Lett.*, 2012, **12**, 3512–3517.

12 M. Drögeler, F. Volmer, M. Wolter, B. Terrés, K. Watanabe, T. Taniguchi, G. Güntherodt, C. Stampfer and B. Beschoten, *Nano Lett.*, 2014, **14**, 6050–6055.

13 S. Roche and S. O. Valenzuela, *J. Phys. D. Appl. Phys.*, 2014, **47**, 094011.

14 M. V. Kamalakar, C. Groenveld, A. Dankert and S. P. Dash, *Nat. Commun.*, 2015, **6**, 6766.

15 M. Drogöler, C. Franzen, F. Volmer, T. Pohlmann, L. Banszerus, M. Wolter, K. Watanabe, T. Taniguchi, C. Stampfer and B. Beschoten, *Nano Lett.*, 2016, **16**, 3533–3539.

16 S. Roche, J. Åkerman, B. Beschoten, J.-C. Charlier, M. Chshiev, S. Prasad Dash, B. Dlubak, J. Fabian, A. Fert, M. Guimarães, F. Guinea, I. Grigorieva, C. Schönenberger, P. Seneor, C. Stampfer, S. O. Valenzuela, X. Waintal and B. J. van Wees, *2D Mater.*, 2015, **2**, 30202.

17 J. Balakrishnan, G. K. W. Koon, A. Avsar, Y. Ho, J. H. Lee, M. Jaiswal, S.-J. Baeck, J.-H. Ahn, A. Ferreira, M. A. Cazalilla, A. H. C. Neto and B. Özyilmaz, *Nat. Commun.*, 2014, **5**, 4748.

18 A. Avsar, J. Y. Tan, T. Taychatanapat, J. Balakrishnan, G. K. W. Koon, Y. Yeo, J. Lahiri, A. Carvalho, A. S. Rodin, E. C. T. O'Farrell, G. Eda, A. H. Castro Neto, B. Özyilmaz, E. O'Farrell, G. Eda, A. H. Castro Neto and B. Özyilmaz, *Nat. Commun.*, 2014, **5**, 4875.

19 E. C. T. O'Farrell, A. Avsar, J. Y. Tan, G. Eda and B. Özyilmaz, *Nano Lett.*, 2015, **15**, 5682–5688.

20 A. Avsar, J. Hak Lee, G. K. W. Koon and B. Özyilmaz, *2D Mater.*, 2015, **2**, 044009.

21 Z. Wang, D. Ki, H. Chen, H. Berger, A. H. MacDonald and A. F. Morpurgo, *Nat. Commun.*, 2015, **6**, 8339.

22 J. B. Mendes, O. Alves Santos, L. M. Meireles, R. G. Lacerda, L. H. Vilela-Leão, F. L. Machado, R. L. Rodríguez-Suárez, A. Azevedo and S. M. Rezende, *Phys. Rev. Lett.*, 2015, **115**, 226601.

23 W. Yan, O. Txoperena, R. Llopis, H. Dery, L. E. Hueso and F. Casanova, *Nat. Commun.*, 2016, **7**, 13372.

24 Z. Wang, D.-K. K. Ki, J. Y. Khoo, D. Mauro, H. Berger, L. S. Levitov and A. F. Morpurgo, *Phys. Rev. X*, 2016, **6**, 041020.

25 A. Dankert and S. P. Dash, *Nat. Commun.*, 2017, **8**, 16093.

26 B. Yang, M. Lohmann, D. Barroso, I. Liao, Z. Lin, Y. Liu, L. Bartels, K. Watanabe, T. Taniguchi and J. Shi, *Phys. Rev. B - Condens. Matter Mater. Phys.*, 2017, **96**, 041409.

27 A. Cresti, D. Van Tuan, D. Soriano, A. W. Cummings and S. Roche, *Phys. Rev. Lett.*, 2014, **113**, 246603.

28 A. Cresti, B. K. Nikolíc, J. H. Garćia and S. Roche, *Riv. Nuovo Cim.*, 2016, **39**, 587–667.

29 P. Tien Vo, N. R. Walet and F. Guinea, *2D Mater.*, 2017.

30 A. Dyrdał and J. Barnaś, *2D Mater.*, 2017, **4**, 034003.

31 C. L. Kane and E. J. Mele, *Phys. Rev. Lett.*, 2005, **95**, 226801.

32 J. Sinova, S. O. Valenzuela, J. Wunderlich, C. H. Back and T. Jungwirth, *Rev. Mod. Phys.*, 2015, **87**, 1213–1260.

33 C. Ertler, S. Konschuh, M. Gmitra and J. Fabian, *Phys. Rev. B - Condens. Matter Mater. Phys.*, 2009, **80**, 041405.

34 D. Huertas-Hernando, F. Guinea and A. Brataas, *Phys. Rev. Lett.*, 2009, **103**, 146801.

35 Y. Zhou and M. W. Wu, *Phys. Rev. B - Condens. Matter Mater. Phys.*, 2010, **82**, 085304.

36 I. Žutić, J. Fabian, S. Das Sarma and S. D. Sarma, *Rev. Mod. Phys.*, 2004, **76**, 323–410.

37 R. J. Elliott, *Phys. Rev.*, 1954, **96**, 266–279.

38 Y. Yafet, *Solid State Phys. - Adv. Res. Appl.*, 1963, **14**, 1–98.

39 H. Ochoa, A. H. Castro Neto and F. Guinea, *Phys. Rev. Lett.*, 2012, **108**, 206808.

40 M. I. Dyakonov and V. I. Perel, *Sov. Phys. Solid State, Ussr*, 1972, **13**, 3023–3026.

41 F. J. Jedema, H. B. Heersche, A. T. Filip, J. J. A. Baselmans and B. J. van Wees, *Nature*, 2002, **416**, 713–716.

42 J. Fabian, A. Matos-Abiague, C. Ertler, P. Stano and I. Zutic, *Acta Phys. Slovaca*, 2007, **57**, 21046.

43 M. W. Wu, J. H. Jiang and M. Q. Weng, *Phys. Rep.*, 2010, **493**, 61–236.

44 N. Tombros, C. Jozsa, M. Popinciuc, H. T. Jonkman and B. J. van Wees, *Nature*, 2007, **448**, 571–574.

45 N. Tombros, S. Tanabe, A. Veligura, C. Jozsa, M. Popinciuc, H. T. Jonkman and B. J. van Wees, *Phys. Rev. Lett.*, 2008, **101**, 46601.

46 C. Józsa, T. Maassen, M. Popinciuc, P. J. Zomer, A. Veligura, H. T. Jonkman and B. J. van Wees, *Phys. Rev. B - Condens. Matter Mater. Phys.*, 2009, **80**, 241403.

47 W. Han and R. K. Kawakami, *Phys. Rev. Lett.*, 2011, **107**, 047207.

48 A. Avsar, T.-Y. Yang, S. Bae, J. Balakrishnan, F. Volmer, M. Jaiswal, Z. Yi, S. R. Ali, G. GÃijntherodt, B. H. Hong, B. Beschoten and B. ÃŰzyilmaz, *Nano Letters*, 2011, **11**, 2363–2368.

49 P. J. Zomer, M. H. D. Guimarães, N. Tombros and B. J. van Wees, *Phys. Rev. B - Condens. Matter Mater. Phys.*, 2012, **86**, 161416.

50 I. Neumann, J. Van De Vondel, G. Bridoux, M. V. Costache, F. Alzina, C. M. S. Torres and S. O. Valenzuela, *Small*, 2013, **9**, 156–160.

51 M. H. D. Guimarães, P. J. Zomer, J. Ingla-Aynés, J. C. Brant, N. Tombros and B. J. van Wees, *Phys. Rev. Lett.*, 2014, **113**, 86602.

52 S. Singh, J. Katoch, J. Xu, C. Tan, T. Zhu, W. Amamou, J. Hone and R. Kawakami, *Appl. Phys. Lett.*, 2016, **109**, 122411.

53 M. Drögeler, L. Banszerus, F. Volmer, T. Taniguchi, K. Watanabe, B. Beschoten and C. Stampfer, *Appl. Phys. Lett.*, 2017, **111**, 122411.

54 M. B. Lundeberg, R. Yang, J. Renard and J. A. Folk, *Phys. Rev. Lett.*, 2013, **110**, 156601.

55 D. Kochan, M. Gmitra and J. Fabian, *Phys. Rev. Lett.*, 2014, **112**, 116602.

56 D. Soriano, D. Van Tuan, S. M. M. Dubois, M. Gmitra, A. W. Cummings, D. Kochan, F. Ortmann, J.-C. Charlier, J. Fabian and S. Roche, *2D Mater.*, 2015, **2**, 022002.

57 D. V. Tuan, F. Ortmann, D. Soriano, S. O. Valenzuela and S. Roche, *Nat. Phys.*, 2014, **10**, 857–863.

58 D. Van Tuan, F. Ortmann, A. W. Cummings, D. Soriano and S. Roche, *Sci. Rep*, 2016, **6**, 21046.

59 A. W. Cummings and S. Roche, *Phys. Rev. Lett.*, 2016, **116**, 086602.

60 Y. A. Bychkov and E. I. Rashba, *J. Phys. C Solid State Phys.*, 1984, **17**, 6039–6045.

61 B. Raes, J. E. Scheerder, M. V. Costache, F. Bonell, J. F. Sierra, J. Cuppens, J. Van de Vondel and S. O. Valenzuela, *Nat. Commun.*, 2016, **7**, 11444.

62 B. Raes, A. W. Cummings, F. Bonell, M. V. Costache, J. F. Sierra, S. Roche and S. O. Valenzuela, *Phys. Rev. B - Condens. Matter Mater. Phys.*, 2017, **95**, 085403.

63 Y. Wang, X. Cai, J. Reutt-Robey and M. S. Fuhrer, *Phys. Rev. B - Condens. Matter Mater. Phys.*, 2015, **92**, 161411.

64 B. Yang, M.-F. Tu, J. Kim, Y. Wu, H. Wang, J. Alicea, R. Wu, M. Bockrath and J. Shi, *2D Mater.*, 2016, **3**, 31012.

65 T. S. Ghiasi, J. Ingla-Aynés, A. A. Kaverzin and B. J. van Wees, *Nano Lett.*, 2017.

66 L. A. Benítez, J. F. Sierra, W. Savero Torres, A. Arrighi, F. Bonell, M. V. Costache and S. O. Valenzuela, *Nat. Phys.*, 2017.

67 T. Wakamura, F. Reale, P. Palczynski, S. Guéron, C. Mattevi and H. Bouchiat, *ArXiv:1710.07483*, 2017.

68 S. Zihlmann, A. W. Cummings, J. H. Garcia, K. Watanabe, T. Taniguchi, C. Schönenberger and P. Makk, *Prep.*

69 E. McCann, K. Kechedzhi, V. I. Fal'ko, H. Suzuura, T. Ando and B. L. Altshuler, *Phys. Rev. Lett.*, 2006, **97**, 146805.

70 D. Van Tuan, J. M. Marmolejo-Tejada, X. Waintal, B. K. Nikolic and S. Roche, *Phys. Rev. Lett.*, 2016, **117**, 176602.

71 M. Ribeiro, S. R. Power, S. Roche, L. E. Hueso and F. Casanova, *ArXiv:1706.02539*, 2017.

72 J. M. Marmolejo-Tejada, J. H. García, P. H. Chang, X. L. Sheng, A. Cresti, S. Roche and B. K. Nikolic, *ArXiv:1706.09361*, 2017.

73 E. McCann, V. I. Fal'ko, V. I. Fal'ko, K. Kechedzhi, V. I. Fal'ko, H. Suzuura, T. Ando, B. L. Altshuler and V. I. Fal'ko, *Phys. Rev. Lett.*, 2012, **108**, 166606.

74 M. Gmitra, D. Kochan, P. Högl and J. Fabian, *Phys. Rev. B - Condens. Matter Mater. Phys.*, 2016, **93**, 155104.

75 A. M. Alsharari, M. M. Asmar and S. E. Ulloa, *Phys. Rev. B - Condens. Matter Mater. Phys.*, 2016, **94**, 241106.

76 A. W. Cummings, J. H. Garcia, J. Fabian and S. Roche, *Phys. Rev. Lett.*, 2017, **119**, 206601.

77 D. Kochan, S. Irmer and J. Fabian, *Phys. Rev. B - Condens. Matter Mater. Phys.*, 2017, **95**, 165415.

78 T. Völkl, T. Rockinger, M. Drienovsky, K. Watanabe, T. Taniguchi, D. Weiss and J. Eroms, *Phys. Rev. B - Condens. Matter Mater. Phys.*, 2017, **96**, 125405.

79 E. McCann and M. Koshino, *Rep. Prog. Phys*, 2013, **76**, 056503.

80 Y.-Y. Y. Zhang, J. Hu, B. A. Bernevig, X. R. Wang, X. C. Xie and W. M. Liu, *Phys. Rev. Lett.*, 2009, **102**, 106401.

81 M. Johnson and R. H. Silsbee, *Phys. Rev. Lett.*, 1985, **55**, 1790.

82 G.-B. Liu, W.-Y. Shan, Y. Yao, W. Yao and D. Xiao, *Phys. Rev. B - Condens. Matter Mater. Phys.*, 2013, **88**, 085433.

83 S. Omar and B. J. van Wees, *Phys. Rev. B - Condens. Matter Mater. Phys.*, 2017, **95**, 081404(R).

84 S. Omar and B. J. van Wees, *arXiv:1711.10293*, 2017.

85 E. Abrahams, P. W. Anderson, D. C. Licciardello and T. V. Ramakrishnan, *Phys. Rev. Lett.*, 1979, **42**, 673.

86 S. Hikami, A. I. Larkin and Y. Nagaoka, *Prog. Theor. Phys.*, 1980, **63**, 707–710.

87 B. L. Altshuler, D. Khmel'nitzkii, A. I. Larkin and P. A. Lee, *Phys. Rev. B - Condens. Matter Mater. Phys.*, 1980, **22**, 5142.

88 Y. A. Bychov and E. I. Rashba, *Pis'ma Eksp. Teor. Fiz.*, 1984, **39**, 66.

89 J. H. Garcia, A. W. Cummings and S. Roche, *Nano Lett.*, 2017, **17**, 5078–5083.

90 D. Xiao, M. C. Chang and Q. Niu, *Rev. Mod. Phys.*, 2010, **82**,

1959–2007.
91 D. J. Thouless, M. Kohmoto, M. P. Nightingale and M. Den Nijs, *Phys. Rev. Lett.*, 1982, **49**, 405.
92 J. H. Garcia and T. G. Rappoport, *2D Mater.*, 2016, **3**, 024007.
93 O. V. Dimitrova, *Phys. Rev. B - Condens. Matter Mater. Phys.*, 2005, **71**, 245327.
94 M. Milletarì, M. Offidani, A. Ferreira and R. Raimondi, *Phys. Rev. Lett.*, 2017.
95 A. Isacsson, A. W. Cummings, L. Colombo, L. Colombo, J. M. Kinaret and S. Roche, *2D Mater.*, 2017, **4**, 12002.
96 J. Balakrishnan, G. Kok Wai Koon, M. Jaiswal, A. H. Castro Neto and B. Özyilmaz, *Nat. Phys.*, 2013, **9**, 284–287.
97 D. A. Abanin, A. V. Shytov, L. S. Levitov and B. I. Halperin, *Phys. Rev. B - Condens. Matter Mater. Phys.*, 2009, **79**, 035304.
98 W. Savero Torres, J. F. Sierra, L. A. Benítez, F. Bonell, M. V. Costache and S. O. Valenzuela, *2D Mater.*, 2017, **4**, 041008.
99 J.-i. Inoue, G. E. W. Bauer and L. W. Molenkamp, *Phys. Rev. B - Condens. Matter Mater. Phys.*, 2003, **67**, 033104.
100 A. Manchon and S. Zhang, *Phys. Rev. B - Condens. Matter Mater. Phys.*, 2009, **79**, 094422.
101 I. Mihai Miron, G. Gaudin, S. Auffret, B. Rodmacq, A. Schuhl, S. Pizzini, J. Vogel and P. Gambardella, *Nat. Mater.*, 2010.
102 P. Gambardella and I. M. Miron, *Philos. Trans. R. Soc. A Math. Phys. Eng. Sci.*, 2011, **369**, 3175–3197.
103 K. Garello, I. M. Miron, C. O. Avci, F. Freimuth, Y. Mokrousov, S. Blügel, S. Auffret, O. Boulle, G. Gaudin and P. Gambardella, *Nat. Nanotechnol.*, 2013, **8**, 587–593.
104 A. Dyrdał, J. Barnaś and V. K. Dugaev, *Phys. Rev. B - Condens. Matter Mater. Phys.*, 2014, **89**, 4404.
105 A. Dyrdał and J. Barnaś, *Phys. Rev. B - Condens. Matter Mater. Phys.*, 2015, **92**, 165404.
106 S. Takahashi and S. Maekawa, *Sci. Technol. Adv. Mater*, 2008, **9**, 014105.
107 K. Song *et al.*, *in preparation*.